Wavelength selection and symmetry breaking in orbital wave ripples

Citation: Nienhuis, Jaap H., J. Taylor Perron, Justin C. T. Kao, and Paul M. Myrow. "Wavelength Selection and Symmetry Breaking in Orbital Wave Ripples." J. Geophys. Res. Earth Surf. 119, no. 10 (October 2014): 2239–2257. © 2014 American Geophysical Union

As Published: http://dx.doi.org/10.1002/2014JF003158

Publisher: American Geophysical Union (AGU)

Persistent URL: http://hdl.handle.net/1721.1/97905

Version: Final published version: final published article, as it appeared in a journal, conference proceedings, or other formally published context

AGU PUBLICATIONS

JGR

Journal of Geophysical Research: Earth Surface

RESEARCH ARTICLE
10.1002/2014JF003158

Key Points:
- Maximum flow separation length sets equilibrium orbital ripple wavelength
- Equilibrium ripple wavelength maximizes upslope sand flux by separation vortices
- Fluid dynamical effects break the symmetry of transiently adjusting ripples

Supporting Information:
- Readme
- Movie S1
- Movie S2
- Movie S3
- Movie S4
- Movie S5
- Movie S6

Correspondence to:
J. H. Nienhuis,
jhn@mit.edu

Citation:
Nienhuis, J. H., J. T. Perron, J. C. T. Kao, and P. M. Myrow (2014), Wavelength selection and symmetry breaking in orbital wave ripples, *J. Geophys. Res. Earth Surf.*, *119*, 2239–2257, doi:10.1002/2014JF003158.

Received 31 MAR 2014
Accepted 16 SEP 2014
Accepted article online 18 SEP 2014
Published online 20 OCT 2014

Wavelength selection and symmetry breaking in orbital wave ripples

Jaap H. Nienhuis[1,2], J. Taylor Perron[1], Justin C. T. Kao[1,3], and Paul M. Myrow[4]

[1]Department of Earth, Atmospheric and Planetary Sciences, Massachusetts Institute of Technology, Cambridge, Massachusetts, USA, [2]Geology and Geophysics Department, Woods Hole Oceanographic Institution, Woods Hole, Massachusetts, USA, [3]Dropbox Inc., San Francisco, California, USA, [4]Department of Geology, Colorado College, Colorado Springs, Colorado, USA

Abstract Sand ripples formed by waves have a uniform wavelength while at equilibrium and develop defects while adjusting to changes in the flow. These patterns arise from the interaction of the flow with the bed topography, but the specific mechanisms have not been fully explained. We use numerical flow models and laboratory wave tank experiments to explore the origins of these patterns. The wavelength of "orbital" wave ripples (λ) is directly proportional to the oscillating flow's orbital diameter (d), with many experimental and field studies finding $\lambda/d \approx 0.65$. We demonstrate a coupling that selects this ratio: the maximum length of the flow separation zone downstream of a ripple crest equals λ when $\lambda/d \approx 0.65$. We show that this condition maximizes the growth rate of ripples. Ripples adjusting to changed flow conditions develop defects that break the bed's symmetry. When d is shortened sufficiently, two new incipient crests appear in every trough, but only one grows into a full-sized crest. Experiments have shown that the same side (right or left) wins in every trough. We find that this occurs because incipient secondary crests slow the flow and encourage the growth of crests on the next flank. Experiments have also shown that when d is lengthened, ripple crests become increasingly sinuous and eventually break up. We find that this occurs because crests migrate preferentially toward the nearest adjacent crest, amplifying any initial sinuosity. Our results reveal the mechanisms that form common wave ripple patterns and highlight interactions among unsteady flows, sediment transport, and bed topography.

1. Introduction

1.1. Orbital Wave Ripples

Sand ripples in coastal environments (Figure 1a) and the rock record are a ubiquitous signature of the interaction of flows, bed topography, and sediment transport. Water particles under surface gravity waves move in nearly closed circular paths, which become increasingly elliptical closer to the bed. The resulting oscillatory flow over the bed generates symmetric ripples, which display a wide range of geometric characteristics [*Miller and Komar*, 1980; *Pedocchi and García*, 2009a]. Oscillatory flow ripples that are created and sustained by vortices on the lee sides of ripple crests (Figure 1b) are termed vortex ripples [*Bagnold and Taylor*, 1946]. Here we focus on orbital wave ripples, a common class of vortex ripples, which exhibit a well-known linear relationship between the wavelength of the ripple pattern and the orbital diameter (twice the amplitude) of the water particles [*Nielsen*, 1981; *Wiberg and Harris*, 1994]. Because the orbital diameter depends on the water depth and the height and length of the waves, the ripple wavelength is often used as a paleoenvironmental indicator [*Clifton and Dingler*, 1984]. In addition, the height and spacing of modern ripples are major controls on bed roughness [*Grant and Madsen*, 1982].

In addition to equilibrium morphology, orbital wave ripples commonly display characteristic patterns during their transient evolution [*Evans*, 1949]. Ripples evolve on time scales of minutes to hours, often leaving ripple fields in disequilibrium with respect to quickly changing wave conditions (for example, storms) or water depths (for example, tides) [*Traykovski et al.*, 1999]. A better understanding of the morphology of transient ripple fields will enable improved paleoenvironmental reconstructions and aid the development of morphologic models. Here we focus on the fluid dynamical controls on the equilibrium ripple wavelength and the transient patterns that emerge as ripples adjust to changes in the oscillatory flow.

1.2. Previous Studies of Wave Ripple Morphodynamics

1.2.1. Ripple Growth and Flow Characteristics

Bagnold and Taylor [1946] studied the role of vortices in the process of ripple formation. When flow over a sand bed is strong enough to move the grains, the grains begin to roll back and forth over the initially

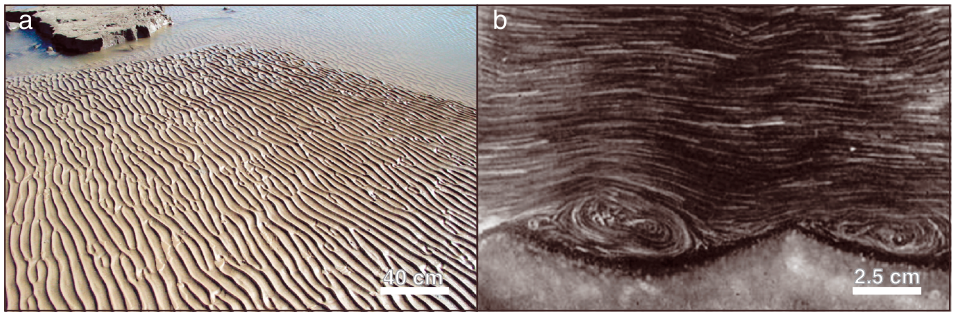

Figure 1. (a) Ripples on a beach at low tide at Sea Rim State Park, Texas. Photo by Zoltán Sylvester. Scale bar is approximate due to perspective. (b) Flow over ripples, visualized with tracers. Instantaneous flow high above the bed is to the right, with clockwise rotating vortices extending from the lee sides of the ripples. Reproduced from *Bagnold and Taylor* [1946].

flat bed, forming mobile, parallel bands of roughly triangular "rolling grain ripples." A hydrodynamic instability that generates coherent flow structures can also contribute to the formation of incipient ripples on an initially flat bed [*Cappietti and Chopart*, 2006]. As the ripples collect more grains, grow taller, and become more stationary, the flow separates from the bed at the crests, and vortices grow on the lee sides of the crests (Figure 1b) [*Bagnold and Taylor*, 1946]. In the region between the separated flow and the bed, known as the separation zone, a vortex forms that typically drives flow near the bed in a direction opposite to the average flow high above the bed. The diameter of the vortex is comparable to, but smaller than, the separation length, which is the horizontal distance between the separation point (approximately at the ripple crest) and the flow reattachment point (Figure 2a). In the separation zone, which grows and disappears during each wave half cycle, the reversed flow moves sediment upstream toward the crest (Figure 2b, top). When the flow reverses halfway through the orbital cycle, the entire vortex is carried back up the crest, ejected off the top of the crest, and then advected up away from the bed [*Longuet-Higgins*, 1981] (Figure 2b, bottom). Any suspended sediment carried by the vortex is released as the vortex dissipates higher up in the flow and settles into the trough [*Scherer et al*., 1999].

1.2.2. Equilibrium Ripple Form

Numerous experiments and field observations have shown that the wavelength of orbital wave ripples, λ, scales linearly with the orbital diameter of the flow, d [*Wiberg and Harris*, 1994]:

$$\lambda \approx 0.65d, \tag{1}$$

and is independent of the wave period [*Nielsen*, 1981]. In highly energetic flows, the proportionality coefficient in equation (1) declines below 0.65 as sediment becomes more mobile [*Nielsen*, 1981; *Pedocchi and García*, 2009a, 2009b], but the orbital diameter is still the primary control on the ripple wavelength. Here we focus on flows that give rise to the commonly observed ratio of $\lambda/d \approx 0.65$.

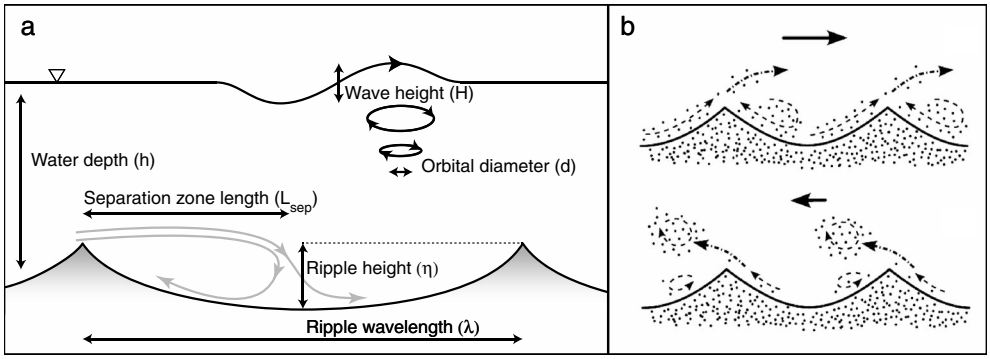

Figure 2. (a) Illustration of the terminology used to describe flow over ripples. Diagrams are not to scale. (b) Schematic drawing of the sediment transport at maximum flow velocity (top) and soon after flow reversal (bottom). Reproduced from *Pedocchi and García* [2009a].

Ripples grow until the sediment flux upward toward the crest is balanced by avalanching, which maintains angle-of-repose slopes on either side of each crest. This leads to a consistent ratio between the ripple height, η, and the ripple wavelength [*Nielsen*, 1981]. This ratio is commonly referred to as the ripple steepness. Average ripple steepness values reported in the literature vary slightly among studies, but an extensive recent compilation [*Pedocchi and García*, 2009a] indicates that the most typical value for orbital ripples is

$$\eta/\lambda \approx 0.15. \tag{2}$$

Previous studies of flow over ripples have suggested partial explanations for this equilibrium ripple geometry. *Longuet-Higgins* [1981] showed mathematically that a peak in the drag coefficient occurs on a rippled bed with λ/d close to 0.65. *Scherer et al*. [1999] noted that, during each half wave cycle, the center of the separation vortex growing from a ripple crest travels to a position approximately halfway to the next ripple crest. Other studies, most notably that of *Andersen* [1999], explored the impact of the separation vortex on bed shear stress patterns. *Andersen* [1999] found that small orbital diameters produce separation zones that do not reach the trough and therefore cannot transport a significant amount of sediment from troughs to crests. However, it is not clear how these effects drive ripples to their equilibrium wavelength.

1.2.3. Transient Ripple Adjustment

Early laboratory studies of the adjustment of ripples to changes in orbital diameter revealed transient morphologies such as splitting crests and the appearance of new incipient crests (commonly referred to as secondary crests, Figure 3a) in each trough in response to decreased wave intensity [*Evans*, 1943, 1949; *Shulyak*, 1963]. Experiments by *Lofquist* [1978] and *Sekiguchi and Sunamura* [2004] related the particular transient morphologies to the magnitude of the decrease in the orbital diameter of the flow. Most crests show simple translational migration ("sliding") if the new d is between 80% and 100% of the original d [*Smith and Sleath*, 2005]. For larger reductions in d, secondary crests accommodate shortening of the ripple wavelength [*Lofquist*, 1978], a process that involves several stages. A pair of new, small crests initially appears on the flanks of each ripple, one on either side of the original crest [*Schnipper et al*., 2008]. Very quickly thereafter, the trough flattens and the new crests, which by this time have formed their own small separation vortices, migrate toward the center of the trough [*Marieu et al*., 2008]. In cases where the new equilibrium spacing would not sustain two new ripples in each trough, one crest grows and the other decays. For some reason, the same side wins in every trough throughout the ripple field: either all "right-sided" or all "left-sided" secondary crests grow (Figure 3a) [*Sekiguchi*, 2005; *Schnipper et al*., 2008]. *Sekiguchi* [2005] attributed this phenomenon to asymmetric drift in the wave orbital motion. However, later experiments by *Schnipper et al*. [2008] showed similar patterns in symmetrical flow, indicating that a coupling between the topography and the flow must be responsible.

The nearly straight and level crests associated with equilibrium conditions [*Rubin*, 2012] become unstable for select increases in the orbital diameter (Figure 3b). Increases in the wave orbital diameter cause ripple crests to slide and merge with adjacent ripples [*Doucette and O'Donoghue*, 2006]. *Hansen et al*. [2001] observed a 2-D "bulging" pattern, in which crests become increasingly sinuous and eventually break up and merge with neighboring crests, increasing the average ripple wavelength. Although similarities with Rayleigh-Plateau instabilities, in which a long vortex breaks up into segments, have been suggested [*Hansen et al*., 2001], there have been no systematic investigations of how these transient patterns are related to flow structures.

1.3. Overview

In this paper, we examine how structures that develop in turbulent, oscillatory flows over ripples relate to the equilibrium and transient patterns described above. Although interactions between flows and bed forms are three dimensional, we find that the major features of the observed ripple patterns can be understood by examining the interaction of a two-dimensional flow with a one-dimensional bed elevation profile. We describe laboratory wave tank experiments in which we reproduce and measure the patterns observed in previous studies. We then present numerical simulations of oscillatory flows over observed and synthetic ripple profiles, which we use to investigate flow structures and bed stresses that influence ripple evolution. Our experimental and numerical results show how flow structures set the equilibrium ripple wavelength and produce characteristic defect patterns in ripples with shortening and lengthening wavelengths.

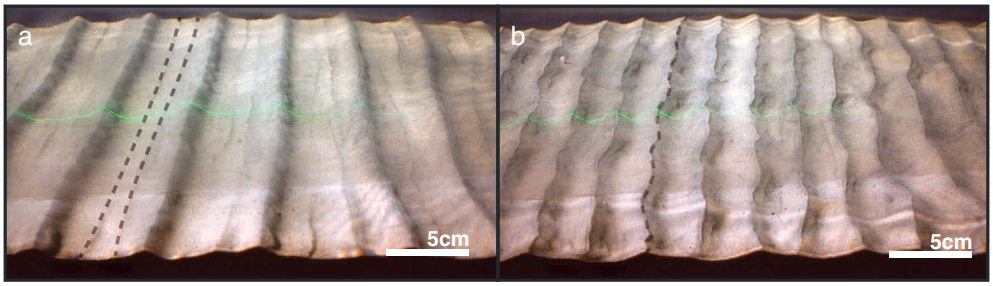

Figure 3. Defects observed during transient ripple adjustment in our laboratory wave tank (see section 2.1 for a description of the experimental setup). (a) Secondary crests forming in response to a shortened orbital diameter. Two new small secondary crests are present in each trough. Dashed lines highlight the secondary crests in one trough. In this experiment, all crests on the right sides of troughs continued growing while the left-sided crests slowly decayed or merged. Initial bed with $\lambda = 0.07$ m was subjected to a flow with $d = 0.05$ m, a shortening factor ($\lambda_{new}/\lambda_{old}$) of 0.46. See Movie S1 in the supporting information. (b) Sinuous crests forming in response to a lengthened orbital diameter. Dashed line highlights an example of a sinuous crest. Initial bed with $\lambda = 0.04$ m was subjected to a flow with $d = 0.12$ m, a lengthening factor ($\lambda_{new}/\lambda_{old}$) of 1.95. See Movie S2.

2. Methods

We conducted experiments in a laboratory wave tank to generate ripples with equilibrium and transiently adjusting wavelengths, and collected real-time video, time-lapse imagery, and time-lapse elevation profiles of the evolving bed. We then used a lattice Boltzmann numerical flow model to calculate stresses over both hypothetical and experimentally observed bed profiles. The combination of these two approaches allowed us to track the hydrodynamic and morphodynamic evolution of ripples.

2.1. Wave Tank Experiments

We used a laboratory wave tank (Figure 4a) to investigate the evolution of wave ripples under controlled conditions. The tank is 60 cm wide × 50 cm deep × 7 m long. At one end, a hinged paddle attached to a motor oscillates and produces waves. At the opposite end, an artificial beach made of rubberized horsehair damps these waves, preventing interference from reflected waves. A 5 cm thick layer of sediment (median diameter $D_{50} = 0.18$ mm) covers the bottom of the tank. In the absence of waves and ripples, the height of the water surface above the top of the sand bed is 40 cm. An overflow head tank connected to the main tank with a tube maintains a constant water level.

A central section of the tank about 60 centimeters long in the wave propagation direction was imaged at close range from an oblique angle with real-time video and time-lapse images triggered every 10 wave cycles. We projected a green line on the bed parallel to the wave propagation direction with a laser sheet mounted on an overhead boom (Figure 4b). This line can be extracted easily from the captured photos by finding peaks in the intensity of the green image band. To convert the extracted image profile to a bed elevation profile, we multiply the coordinates of the image pixels with a calibrated transformation matrix.

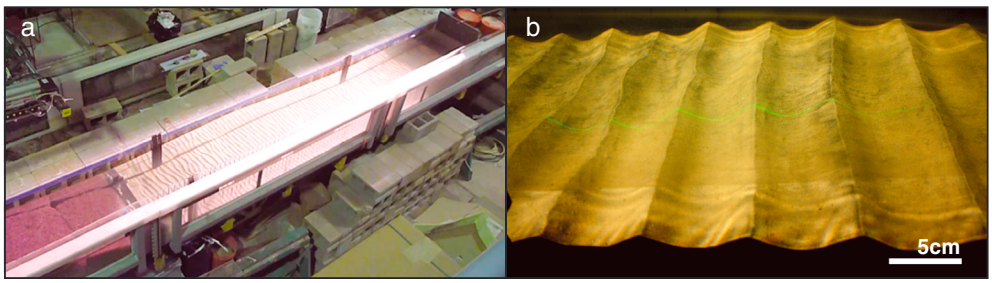

Figure 4. (a) Overhead view of the wave tank. Waves propagate from the paddle at upper right to the wave-damping beach at lower left. Section with sand bed is approximately 5 m long. (b) Typical captured image of the bed showing the green laser line used to extract a bed elevation profile. Wave propagation direction is to the right.

We tune the motor speed and paddle travel distance to produce the desired orbital diameter at the bed. We measure wave period, water depth, and wave height during the experiments and calculate the orbital diameter using linear wave theory. We generate waves with typical heights between 4 and 10 cm and typical periods between 1 and 3 s. This allows us to create orbital diameters between 5 and 15 cm and equilibrium ripple wavelengths between 3 and 10 cm. A typical experiment begins with a level bed superimposed with small, evenly spaced ridges perpendicular to the flow direction to accelerate the initial growth of ripples. The size and spacing of these initial perturbations do not influence the wavelength of the ripples that subsequently grow. After a few hours, the ripple field reaches an equilibrium in which the average wavelength is roughly constant in time. We then select new wave conditions with a different orbital diameter and observe the adjustment toward a new equilibrium.

We performed 11 experiments with adjustment factors ($\lambda_{new}/\lambda_{old}$) ranging from 0.33 (three new crests for every old crest) to 2.7 (about three new crests for every eight old crests). In agreement with earlier observations, secondary crests formed in experiments with $\lambda_{new}/\lambda_{old} < 0.8$ (Figure 3a) [*Sekiguchi and Sunamura*, 2004]. In experiments with $\lambda_{new}/\lambda_{old} > 1$, we observed bulging crests (Figure 3b), crest annihilation and sliding crests. To examine the process of ripple growth more closely, we performed three additional experiments in which we investigated the spreading of ripples from a single initial crest in a flow with $d = 13$ cm.

2.2. Numerical Flow Simulations

2.2.1. Lattice Boltzmann Numerical Flow Model

Rather than implementing a full morphodynamic model, we study the incipient effects of wave-driven flow on ripple evolution by simulating two-dimensional, oscillatory flow over a fixed bed elevation profile and calculating proxies for bed erosion and deposition. We use the lattice Boltzmann method (LBM), which does not solve the Navier-Stokes equations directly but instead models the fluid by moving fictive particle density distributions among nodes on a discrete lattice [*Chen and Doolen*, 1998; *Aidun and Clausen*, 2010]. The LBM has been extensively tested and applied to complex fluid dynamics problems [*Chen and Doolen*, 1998; *Aidun and Clausen*, 2010] and reproduces key flow features observed in ripple morphodynamics, such as flow separation and vortex development (Figure 5) [*Cappietti*, 2006]. Additionally, this method is ideally suited for flow over ripples due to the ease of implementing geometrically irregular boundaries.

The lattice Boltzmann equation for the time evolution of the fictive particle density distributions is

$$f_i(\vec{x} + \vec{e}_i, t+1) = f_i(\vec{x}, t) + \Omega_i(f(\vec{x}, t)) + f_i^{ext}(\vec{x}, t), \tag{3}$$

where $\vec{x}$ is the position vector, t is time in lattice units (defined below), f_i is the particle density distribution function in lattice direction i, $\vec{e}_i$ are the discrete velocity vectors, Ω_i is the collision operator, and $f_i^{ext} = 3w_i\left(\vec{e}_i \cdot \vec{F}\right)$ accounts for externally imposed body forces $\vec{F}$, with the weights w_i defined below. We use a two-dimensional regular lattice in which each local neighborhood includes nine nodes and nine directions (the so-called "D2Q9" model, Figure 5).

The simplest collision operator is the Bhatnagar-Gross-Krook (BGK) operator,

$$\Omega_i(f(\vec{x}, t)) = -\frac{1}{\kappa}\left[f_i(\vec{x}, t) - f_i^{eq}(\vec{x}, t)\right], \tag{4}$$

with a single relaxation time κ. The equilibrium distribution for an incompressible fluid is

$$f_i^{eq}(\vec{x}, t) = \rho w_i\left[1 + \frac{\vec{e}_i \cdot \vec{u}}{c_s^2} + \frac{(\vec{e}_i \cdot \vec{u})^2}{2c_s^4} - \frac{u^2}{2c_s^2}\right], \tag{5}$$

with $w_0 = 4/9$, $w_{1,2,3,4} = 1/9$, $w_{5,6,7,8} = 1/36$, and $c_s = 1/\sqrt{3}$. Macroscopic variables, such as fluid density ρ and momentum $\rho\vec{u}$ (and therefore also velocity $\vec{u}$), can be obtained from the distribution function by

$$\rho = \sum_i f_i, \quad \rho\vec{u} = \sum_i f_i\vec{e}_i. \tag{6}$$

The model based on the BGK collision operator contains spurious modes, which in practice are observed as checkerboard patterns in the solutions. At low Reynolds numbers, these modes have negligible amplitude, but they can become significant at moderate to high Reynolds numbers. In order to obtain a numerically stable

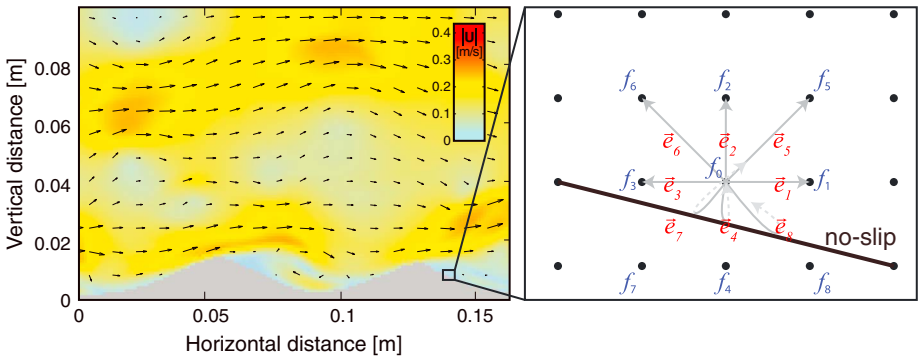

Figure 5. Flow over a bed profile measured in the wave tank, modeled using the lattice Boltzmann method. Solid nodes below the bed surface are colored gray. Colors above the bed indicate the velocity magnitude, and vectors indicate the velocity magnitude and direction. The flow phase is 30°, with 90° and 270° being maximum flow to the right and left, respectively. Flow separation occurs at each ripple crest, and vortices form in the troughs. The inset illustrates the lattice at a location near the bed surface, including the velocity vectors e_i and particle density distribution functions f_i for a representative node. Gray arrows represent the streaming of particle density distributions from the node to its neighbors, with the dashed parts of reversed arrows indicating the "bounce-back" condition used to represent the no-slip boundary.

solution, we turn instead to the multiple relaxation time model, as described by *Lallemand and Luo* [2000, 2003] and *Bouzidi et al.* [2001]. In this approach, collisions are performed in a basis constructed from the moments of the discrete velocity density distribution, and relaxation parameters associated with the nonphysical modes may be chosen to damp out those modes. The moments $\hat{f} = \left(\rho, e, \varepsilon, j_x, q_x, j_y, q_y, p_{xx}, p_{xy}\right)^T$ are obtained from the distribution function by use of a transformation matrix

$$M = \begin{pmatrix} 1 & 1 & 1 & 1 & 1 & 1 & 1 & 1 & 1 \\ -4 & -1 & -1 & -1 & -1 & 2 & 2 & 2 & 2 \\ 4 & -2 & -2 & -2 & -2 & 1 & 1 & 1 & 1 \\ 0 & 1 & 0 & -1 & 0 & 1 & -1 & -1 & 1 \\ 0 & -2 & 0 & 2 & 0 & 1 & -1 & -1 & 1 \\ 0 & 0 & 1 & 0 & -1 & 1 & 1 & -1 & -1 \\ 0 & 0 & -2 & 0 & -2 & 1 & 1 & -1 & -1 \\ 0 & 1 & -1 & 1 & -1 & 0 & 0 & 0 & 0 \\ 0 & 0 & 0 & 0 & 0 & 1 & -1 & 1 & -1 \end{pmatrix}, \tag{7}$$

such that $\hat{f} = Mf$. Here e is related to kinetic energy; ε to energy squared; j_x, j_y are the momentum density; q_x, q_y are proportional to the energy flux; and p_{xx}, p_{xy} are proportional to the diagonal and off-diagonal components of the viscous stress tensor. Then, the collision is performed according to

$$\Omega_i(f(\vec{x},t)) = -M^{-1}S\left[\hat{f}_i(\vec{x},t) - \hat{f}_i^{\mathrm{eq}}(\vec{x},t)\right], \tag{8}$$

where $S = \mathrm{diag}(0, s_2, s_3, 0, s_5, 0, s_7, s_8, s_9)$ are the relaxation parameters, and the equilibrium moments are given by $e^{\mathrm{eq}} = -2\rho + (3/\rho)\left(j_x^2 + j_y^2\right), \varepsilon^{\mathrm{eq}} = \rho - (3/\rho)\left(j_x^2 + j_y^2\right), q_x^{\mathrm{eq}} = -j_x, q_y^{\mathrm{eq}} = -j_y, p_{xx}^{\mathrm{eq}} = (1/\rho)\left(j_x^2 - j_y^2\right)$, and $p_{xy}^{\mathrm{eq}} = (1/\rho)\left(j_x j_y\right)$. Only s_8 and s_9 have physical meaning here; they are expressed in terms of the viscous relaxation time: $s_8 = s_9 = 1/\kappa$. The remaining relaxation parameters may be tuned to damp the nonphysical modes of the lattice Boltzmann scheme. In this work, we take $s_2 = s_3 = s_5 = s_7 = 1.1$.

In a fully resolved calculation, κ would correspond to the molecular viscosity. Such calculations are impractical for most macroscopic flow problems, however, and so we follow many previous modeling efforts

and use a large-eddy simulation, as described by *Dong et al*. [2008]. In this approach, the relaxation time κ is modified as

$$\kappa = \frac{1}{2}\left(\kappa_0 + \sqrt{\kappa_0^2 + \frac{18|Q|C^2}{\rho}}\right), \tag{9}$$

with $\kappa_0 = \frac{1}{2} + 3\nu_0$ the molecular relaxation time, $C = 0.18$ the Smagorinsky coefficient, $Q = \sqrt{2Q_{ij}Q_{ij}}$, and $Q_{ij} = \sum_k e_{k,i}e_{k,j}\left(f_k - f_k^{\mathrm{eq}}\right)$ the nonequilibrium stress tensor.

Simulations are conducted in a rectangular, horizontally periodic domain (Figure 5). The top boundary condition is free slip, implemented as specular reflection of the distribution function. This boundary represents a location sufficiently high above the bed that the flow is effectively horizontal. At the bottom boundary, which represents the topography of the sand bed, a drag condition would typically be imposed in order to account for boundary roughness [*Cabot and Moin*, 2000; *Piomelli and Balaras*, 2002; *Piomelli*, 2008; *Chou and Fringer*, 2010]. However, stable implementations of these higher-order boundary conditions in lattice Boltzmann simulations at moderate to high Reynolds numbers remain an area of active research. We therefore use the interpolated no-slip condition of *Bouzidi et al*. [2001] and *Lallemand and Luo* [2003] (Figure 5). This boundary condition limits the scalability of the flow simulations, in the sense that the effective boundary roughness is an emergent characteristic of each simulation rather than a parameter we specify directly, but it does not qualitatively affect our results. To emphasize that the bed shear stress is a relative estimate, we normalize the values to an arbitrary maximum in each figure.

Our calculations are performed in nondimensional lattice units, such that the node spacing, time step duration, and mean density are all unity. The relevant physical scales are $\overline{x}$, $\overline{t}$, and $\overline{\rho}$, the dimensional length, time, and density for the corresponding lattice quantities x, t, and ρ. Thus, dimensional physical quantities may be determined as $\widetilde{x} = \overline{x}x$, $\widetilde{t} = \overline{t}t$, $\widetilde{\rho} = \overline{\rho}\rho$, $\widetilde{u} = (\overline{x}/\overline{t})u$, and $\widetilde{F} = \left(\overline{\rho}\overline{x}/\overline{t}^2\right)F$.

We drive the oscillatory flow with a time-periodic body force,

$$F_x(t) = -\rho \cdot \omega_0 u_0 \cos(\omega_0 \cdot t), \tag{10}$$

where ω_0 is the angular frequency and u_0 is the velocity amplitude. This body force differs from the wave-driven pressure field that generates oscillating flows in our wave tank and in nature, but comparisons of our calculated flow fields with previously published laboratory and numerical experiments (Appendix A) indicate that this difference does not interfere with the model's ability to reproduce the important features of the near-bed flow. From linear wave theory, the orbital diameter $d = u_0T/\pi$ is a function of the velocity amplitude and the wave period $T = 2\pi/\omega_0$.

We approximate the bed shear stress (τ_b) using the bed-normal gradient of the bed-parallel velocity,

$$\tau_b = \nu\rho \left.\frac{\mathrm{d}u_{||}}{\mathrm{d}n}\right|_{n=0} \approx \nu\rho \, \frac{u_{||}(n = \Delta n)}{\Delta n}, \tag{11}$$

where n is a distance coordinate normal to the bed, measured positive above the bed, $u_{||}$ is bed-parallel velocity, and Δn is a small distance increment. The finite-difference approximation of the velocity gradient in equation (11) assumes a no-slip boundary condition at the bed. In our numerical calculations, we use $\Delta n = 1$ mm and interpolate the value of $u_{||}$ from the velocities at adjacent lattice points. The bed shear stress serves as a proxy of incipient erosion or deposition, since the rate of bed elevation change due to bed load sediment transport is

$$\frac{\partial \eta}{\partial t} = -\frac{1}{1-\phi}\frac{\partial q_s}{\partial x}, \tag{12}$$

where ϕ is the bed porosity and the volumetric bed load transport flux per unit width q_s is a monotonic (but typically nonlinear) function of τ_b.

The combination of d and T is chosen to fall in the regime in which wave orbital ripples are expected according to the data compilation of *Pedocchi and García* [2009a]. A typical model run uses a domain 200 lattice units wide by 100 lattice units high, with $\overline{x} = 1$ mm, $\overline{t} = 10^{-5}$ s, and $\overline{\rho} = 1$ g cm^{-3}. The domain height is at least 4 times the ripple height in all calculations presented here. We let the simulations spin up for

5 wave cycles and then analyzed the flow over the following 15 oscillations. This spin-up time is based on analyses of the bed shear stress variance, which reaches a steady regime after the first few cycles.

We compared this implementation of the lattice Boltzmann method with analytical, experimental, and numerical studies of hydrodynamics and find that our simulations accurately reproduce flow velocity fields and separation lengths (Appendix A). We additionally tested the sensitivity of flow separation length, a key quantity in our analysis, to grid resolution by varying $\overline{x}$ and grid size and find that separation length is insensitive to grid resolution (Appendix B).

2.2.2. Numerical Flow Experiments

We conducted three sets of numerical experiments to examine how the oscillatory flow influences the equilibrium wavelength and transient adjustment of rippled beds. Some of our experiments used synthetic bed elevation profiles with bed elevation z given by

$$z(x) = \eta(1 - |\sin(\pi x/\lambda)|), \tag{13}$$

where η is chosen according to equation (2), such that $\eta/\lambda = 0.15$. In other experiments, we used bed elevation profiles extracted from the wave tank experiments. For the purpose of calculating bed shear stress (equation (11)), $n(x) = 0$ at $z(x)$.

In the first set of experiments, which was designed to investigate how flow separation and vortex development are related to the equilibrium ripple wavelength, we simulated flows with 5 cm $\leq d \leq$ 40 cm over a bed of identically sized, synthetic ripples with 1 cm $\leq \lambda \leq$ 50 cm. In each simulation, we estimated the maximum length of the separation zone in a typical wave cycle by averaging the bed shear stress profiles in successive wave cycles at the instant when the flow at the ripple crest reverses (a phase of approximately 180°), and measuring the horizontal distance downstream of the ripple crest in which the averaged bed shear stress is directed against the spatially averaged flow.

In the second set of experiments, which was designed to investigate how ripple height influences separation zone length, we used bed profiles extracted from a wave tank experiment in which ripples were allowed to spread from an isolated crest on the bed. We selected two 30 cm profiles separated by 45 min during a stage in the experiment when several new ripples had formed on either side of the original crest. We used the flow parameters measured during the experiment to drive the simulated flow over the extracted profiles and measured the maximum separation zone length using the procedure described above.

In the third set of experiments, which was designed to investigate how incipient defects in the early stages of ripple adjustment influence the bed shear stress and trigger symmetry breaking, we used both synthetic and measured bed profiles. To study symmetry breaking during shortening of the ripple wavelength, we extracted four time-lapse profiles from an experiment showing secondary crest development. To study symmetry breaking during lengthening of the ripple wavelength, we extracted four time-lapse profiles from an experiment showing crest sinuosity and subsequent annihilation. Over each extracted bed profile, we drove a simulated flow with the same oscillatory amplitude and period measured in the wave tank experiments and calculated the bed shear stress throughout each simulation. To complement these experimentally based simulations, we then simulated flow over synthetic bed profiles with idealized transient morphologies similar to those observed in the experiments. For the scenario of shortening ripple wavelength, we added a secondary crest on either side of each ripple crest, but eliminated one of the secondary crests on one ripple to study the effects of this asymmetry on the flow. The simulated flow over this bed corresponded to a ripple wavelength shorter than that of the main crests. For the scenario of lengthening ripple wavelength, we constructed a bed profile consisting of identical, nearly evenly spaced ripple crests, with the exception that one of the crests was slightly shifted horizontally. We forced the simulated flow over this bed with orbital diameters corresponding to the average crest spacing as well as wider crest spacing. As with the experimentally generated beds, we calculated the bed shear stress throughout these simulations.

3. Results and Discussion

3.1. Fluid Dynamical Control of Orbital Wave Ripple Spacing

3.1.1. Equilibrium Ripples

We analyzed the results of the first set of numerical experiments to examine the relationship between the wave orbital diameter and the length of the separation zone downstream of ripple crests. The phase-averaged bed

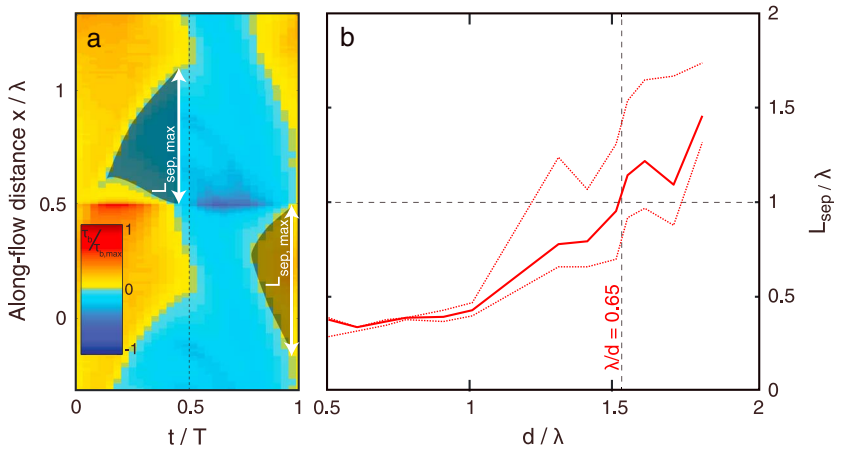

Figure 6. (a) Normalized bed shear stress ($\tau_b/\tau_{b,\max}$) as a function of normalized time (t/T) and normalized distance along the bed (x/λ), averaged over 10 orbital cycles, for a flow with $d/\lambda = 0.95$ ($\lambda/d = 1.05$). The plot covers one wave period and roughly 1.6 ripple wavelengths. The ripple crest is located at $x/\lambda = 0.5$. Mean flow is directed first to the top then to the bottom. The shaded areas mark the separation zones, areas of weak or reversed flow on the lee sides of the crests. The maximum length of the separation zone in this example is 0.7. Note that the bed shear stress reverses slightly before $t/T = 0.5$ because the turbulent boundary layer flow responds to pressure gradients faster than flow farther away from the bed [*Stokes*, 1851]. (b) Plot of median (based on 30 half cycles) separation zone length L_{sep} against orbital diameter d. Both axes are normalized by the ripple wavelength. The dotted lines indicate the 95% confidence interval of the median. The vertical dashed line shows $\lambda/d = 0.65$, the equilibrium ratio observed in compilations of field and laboratory observations.

shear stress over one ripple shows the growth of the separation zone throughout each half wave cycle (Figure 6a). The separation zone reaches its maximum downstream length when the average flow reverses. A plot of the maximum separation length for various d/λ (Figure 6b) shows that larger orbital diameters produce longer separation zones, as expected. Interestingly, when $\lambda/d = 0.65$, the well-known empirical scaling between orbital diameter and ripple wavelength at equilibrium, the maximum separation length extends almost exactly to the next ripple crest. This observation is consistent with the hypothesis that the maximum length of the separation zone controls the ripple wavelength, but it does not explain the mechanism behind the relationship.

We sought a morphodynamic explanation by examining velocity fields and shear stress profiles of flows with λ/d longer and shorter than the equilibrium ratio (Figure 7). If the ratio of ripple wavelength to orbital diameter is smaller than 0.65 (Figure 7a and Movie S3), the flow skims over the crests, and each separation vortex extends beyond the flank and crest of the neighboring ripple. If the ratio of ripple wavelength to orbital diameter is larger than 0.65 (Figure 7c and Movie S5), the separation vortex is strong, but does not extend into the trough, and thus mainly scours the flank of the ripple where it originated. In the case of the equilibrium ratio, $\lambda/d \approx 0.65$ (Figure 7b and Movie S4), the separation vortex is centered on the trough, presumably enhancing sand transport from the trough back toward the crest where the vortex originated (Figure 7b).

To quantify this conceptual explanation for the equilibrium ripple wavelength, we calculated the effect of each flow field on the instantaneous rate of ripple growth. For a flow with $d = 0.077$ m and $T = 2.5$ s over a range of bed profiles with ripple wavelengths of $0.25 \leq \lambda/d \leq 2.5$, we calculated the total bed shear force in the separation zone and divided by the ripple wavelength to obtain an average shear stress per unit width. This serves as a proxy for the upstream sand flux from troughs to crests, and therefore for the growth rate of ripples. This quantity peaks at $\lambda/d \approx 0.65$ (Figure 7d), suggesting that the equilibrium ripple wavelength observed in laboratory experiments and in the field is the wavelength for which flow structures drive the fastest resteepening of the crest after the flattening that occurs during flow acceleration.

We attribute the peak in separation zone shear stress at $\lambda/d = 0.65$ to a resonance between the bed topography and the vortical flow structure [*Longuet-Higgins*, 1981]. In this resonance, the vortex that is ejected up from a ripple crest as the flow reverses (Figure 2b) reinforces the newly created separation vortex in the next (downstream) trough (Movie S4). Shorter and longer λ/d ratios displace the ejected vortex to parts of the flow that do not reinforce the new separation vortex (Movies S3 and S5).

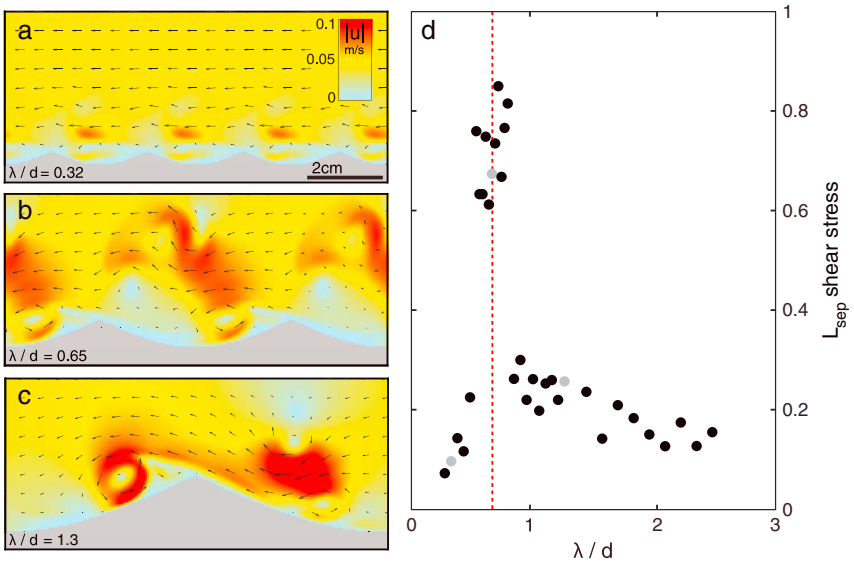

Figure 7. (a) Close-ups of the modeled flow fields at $t/T = 1/3$ for ripples with wavelengths (a) shorter than, (b) equal to, and (c) longer than the equilibrium length of $\lambda/d = 0.65$. Colors and arrows indicate the local velocity magnitude and direction. Arrow lengths have different scales in Figures 7a–7c. Movies S3–S5 in the supporting information illustrate the flows in Figures 7a–7c. (d) The average normalized bed shear stress due to reversed flow, for varying λ/d. The vertical dashed line shows $\lambda/d = 0.65$, the equilibrium ratio observed in compilations of field and laboratory observations. The three grey markers correspond to the scenarios in Figures 7a–7c. All flows have $d = 0.077$ m and $T = 2.5$ s.

3.1.2. Growing Ripples

The preceding analysis suggests that the maximum length of the separation zone, which in turn scales with the flow orbital diameter, controls the equilibrium ripple spacing. However, experimental observations of ripples growing from an initially flat bed indicate that orbital diameter alone does not explain the entire growth history of ripples. *Lofquist* [1978] observed that the spacing and height of incipient ripples grow with time, with the spacing finally reaching the equilibrium wavelength of $0.65d$ when the crests reach the angle of repose.

To test whether our explanation for the equilibrium ripple wavelength is also consistent with growing ripples, we compared the wavelengths and maximum separation lengths of transiently growing ripples. Using the bed profiles extracted from the wave tank experiment in which ripples were allowed to spread from a single initial crest (Figure 8a), we measured ripple height and spacing through time for the original crest and three successive new crests that developed on one side of the original. We then performed flow simulations over bed profiles from two instants in the experiment and calculated the maximum flow separation length for each ripple.

Our results indicate that taller ripples have longer wavelengths and longer separation zones (Figure 8b). Moreover, the maximum separation length and ripple wavelength are approximately equal throughout the process of ripple growth (Figure 8b), suggesting that the wavelengths of developing ripples are set by the same mechanism as equilibrium ripples. During growth, the increase in ripple height lags behind the increase in ripple wavelength. As ripples approach their equilibrium wavelength, their height continues to grow until their flanks reach the angle of repose. Measurements of the steepest slopes on growing crests in the experiment (Figure 8) confirmed that growing crests have gentler slopes than equilibrium crests.

Our results support previous suggestions that the equilibrium orbital ripple wavelength of $\lambda = 0.65d$ results from a resonance condition between vortical flow structures and the rippled bed [*Longuet-Higgins*, 1981; *Scherer et al*., 1999]. Our flow simulations additionally suggest a mechanism by which this resonance influences wave ripple growth: at conditions near equilibrium ($\lambda/d \approx 0.65$), reinforcement of newly formed separation vortices by previously ejected vortices (Figure 2b) maximizes the shear stress associated with reversed flow near the bed (Figure 7b). This peak in shear stress has two main consequences for the interaction of the flow with the bed. First, the associated dissipation of energy likely contributes to the

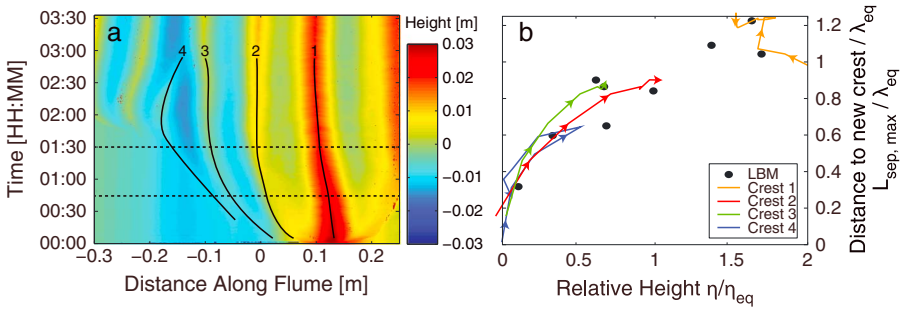

Figure 8. (a) Time series of bed profile height in a wave tank experiment in which a ripple field spreads from a single crest (labeled 1) initially located at an along-flume distance of 0.12 m. $d = 0.13$ m, $T = 2.8$ s. Movie S6 (supporting information) shows a time-lapse animation of the experiment. Numbered black lines trace the positions of ripple crests through time. Dotted lines indicate the two bed profiles used in the LBM simulations. (b) Scaling of crest spacing and maximum separation zone length with ripple height. Colored lines indicate the evolution of crests highlighted in Figure 8a, with arrowheads pointing forward in time. Black points correspond to maximum separation lengths measured in LBM simulations of flow over the bed profiles indicated in Figure 8a.

maximization of form drag for $\lambda/d \approx 0.65$ observed in earlier experiments [*Longuet-Higgins*, 1981, and references therein]. Second, it should maximize the trough-to-crest sand transport that drives ripple growth.

The ripple wavelength coevolves with this resonance, approaching an equilibrium state in which the separation zone reaches across each trough to the next ripple crest before the flow reverses (Figure 6b) and the steepest parts of ripple crests are at the angle of repose (Figure 8b). This explanation is consistent with the results of *Andersen* [1999], who showed that short separation zones associated with orbital diameters shorter than the equilibrium condition are not able to erode the neighboring trough.

Our explanation for the ripple wavelength accounts for hydrodynamics and bed shear stress patterns, but it does not directly explain how the motion of sediment grains shapes ripples. Laboratory experiments indicate that sediment transport mechanics can have a secondary influence on the ripple wavelength. *Nielsen* [1981] showed that λ/d declines gradually with increasing mobility number, a measure of the intensity of sediment motion defined as $u_0^2/[(\rho_s/\rho - 1)gD]$, where ρ_s is sediment grain density, g is gravitational acceleration, and D is grain diameter. This trend, which has been confirmed by more extensive compilations of laboratory and field measurements [*Pedocchi and García*, 2009a, 2009b], may reflect the growing influence of suspended sand transport on ripple morphology. Nonetheless, the observation that bed load transport alone is sufficient to predict ripple migration rates [*Traykovski et al.*, 1999] suggests that our explanation for the ripple wavelength based on bed shear stress is justified.

A mechanistic understanding of the processes that determine the equilibrium ripple wavelength aids paleoenvironmental studies, in particular for interpreting wave ripple geometries that may be absent or uncommon in modern environments [*Allen and Hoffman*, 2005; *Jerolmack and Mohrig*, 2005; *Lamb et al.*, 2012] or wave ripples on other planets [*Squyres et al.*, 2004], where different surface gravity and fluid properties could alter the characteristics of the flow.

3.2. Narrowing Ripple Spacing: Symmetry Breaking in Secondary Crests

In the wave tank experiment in which the orbital diameter and ripple wavelength shortened, two secondary crests appeared in each trough during the initial stages of adjustment, one on the left side and one on the right side (Figures 3a and 9a). As in previous studies, we observed that the crest on the same side, right or left, persists and grows in every trough. This symmetry-breaking process is apparent in the bed profiles in Figure 9a, in which the right-hand crests prevail. A plot of the divergence of bed shear stress based on numerical flow simulations, which serves as a proxy for erosion and deposition (Figure 9b), shows that whereas all the secondary crests are likely to experience deposition, the right-hand crests are associated with steeper gradients in bed shear stress, and therefore faster deposition rates. The subsequent evolution of the bed in the experiment shows that this incipient bed shear stress gradient is a good predictor of bed elevation change. The fact that the ripple spacing and the crest deposition rate increase over time is consistent with our observations.

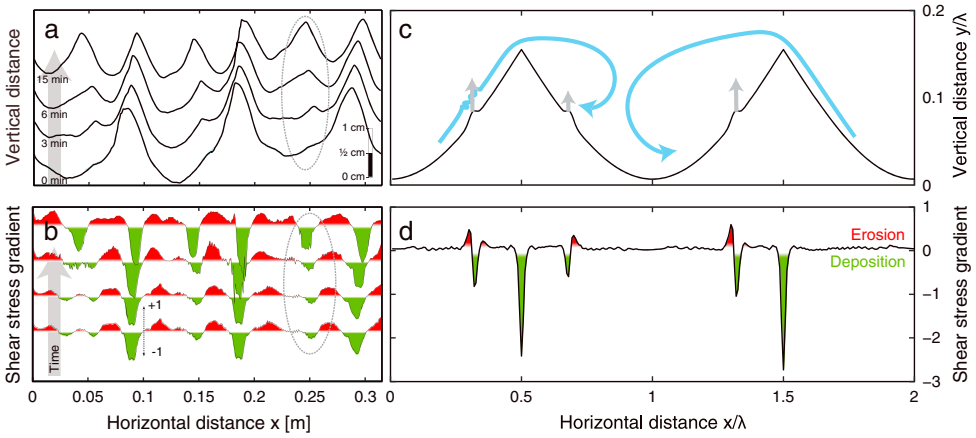

Figure 9. (a) Time sequence of four bed profiles from a wave tank experiment in which the ripple wavelength shortens in response to a shortened orbital diameter (Movie S1 in the supporting information). $\lambda_{new}/\lambda_{old} = 0.47$, $T = 1.28$ s, and $d = 0.05$ m. Time progresses upwards, with profiles from 0, 3, 6, and 15 min after the start of the experiment. (b) Normalized bed shear stress gradient, $d(\tau_b/\tau_{b,max})/dx$, for the profiles in Figure 9a calculated from the numerical flow model. Red- and green-shaded areas indicate incipient erosion and deposition, respectively. The secondary crest inside the dotted ellipse in Figures 9a and 9b grows steadily in an initially symmetrical trough, while the secondary crest on the other side of the trough disappears. (c) Bed profile and (d) normalized bed shear stress gradient in a flow simulation with two primary ripples and three secondary crests. $\lambda/d = 1.07$ in this simulation. Bed shear stress gradients in Figures 9b and 9d are averaged over 10 wave cycles. In Figure 9c, blue lines illustrate schematically the asymmetric streamlines resulting from the secondary crest at far left and the absence of a secondary crest at far right; gray arrows indicate different growth rates of the secondary crests.

A similar flow and stress calculation performed on an idealized bed profile (Figures 9c and 9d) illustrates how an asymmetry in secondary crests in one trough might influence the growth of secondary crests in other troughs. This calculation reveals that each secondary crest acts as a "speed bump," slowing the flow as it ascends a ripple crest and reducing the size of the separation zone that develops on the lee side. This effect, shown schematically by blue flow lines in Figure 9c, influences secondary crest growth in two ways. First, secondary crests on opposite sides of a primary crest compete with one another: a smaller separation zone develops a vortex that scours the leeside ripple flank, interfering with the growth of new crests there. Second, secondary crests on the same sides of adjacent primary crests help one another: the smaller separation zone does not reach the incipient secondary crest on the upstream side of the next ripple, so that incipient crest is not subject to the destructive effects of the vortices in the separation zone. These two mechanisms together create an environment in which either all the left or all the right secondary crests continue to grow.

The shear stress divergence in the idealized scenario (Figure 9d) confirms that an asymmetry in secondary crests in one trough influences the growth rates of secondary crests in adjacent troughs. An unpaired secondary crest on the right-hand side of one trough perturbs the flow sufficiently that the right-hand secondary crest in the adjacent trough experiences faster deposition than the left-hand secondary crest.

After *Sekiguchi* [2005] drew attention to symmetry breaking in secondary crest selection, *Schnipper et al.* [2008] suggested that a hydrodynamical coupling must be involved. Our numerical and experimental results confirm this suggestion and reveal that the influence of secondary crests on flow separation is responsible.

3.3. Widening Ripple Spacing: Amplification of Crest Sinuosity

The nearly straight and level crests of wave ripples in equilibrium with a flow [*Rubin*, 2012] can become unstable for select increases in the orbital diameter. The most prominent instability is the development of sinuous crests during the initial stages of adjustment to a longer ripple wavelength (Figure 3b) as parts of crests initially spaced slightly closer together migrate toward one another and parts of crests initially spaced slightly farther apart migrate away from one another. This process appears to amplify even small initial crest sinuosity.

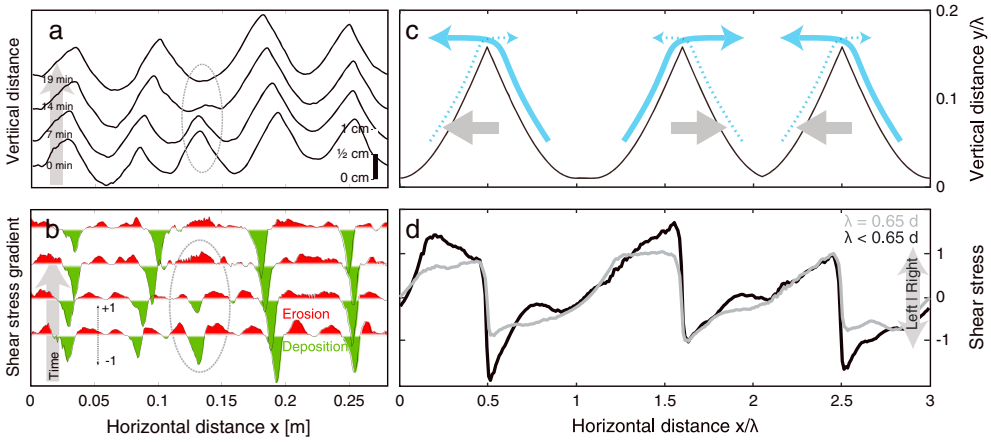

Figure 10. (a) Time sequence of four bed profiles from a wave tank experiment in which the ripple wavelength lengthens in response to a lengthened orbital diameter (Movie S2 in the supporting information). $\lambda_{new}/\lambda_{old} = 2.3$, $T = 2.8$ s, and $d = 0.12$ m. Time progresses upward, with profiles from 0, 7, 14, and 19 min after the start of the experiment. (b) Normalized bed shear stress gradient, $d(\tau_b/\tau_{b,max})/dx$, for the profiles in Figure 10a calculated from the numerical flow model, averaged over 10 wave cycles. Red- and green-shaded areas indicate incipient erosion and deposition, respectively. Dotted ellipse in Figures 10a and 10b highlights the annihilation of a crest. (c) Idealized bed profile with uniform ripple size but uneven ripple spacing. Thickness of blue arrows indicates schematically the magnitude of near-bed velocity in different directions for a flow with $\lambda/d < 0.65$. Gray arrows indicate corresponding ripple migration directions. (d) Normalized bed shear stress, $\tau_b/\tau_{b,max}$, averaged over one wave cycle, for a flow corresponding to equilibrium conditions ($\lambda/d = 0.65$) and a flow that leads to amplified ripple sinuosity ($\lambda/d = 0.36$).

A flow calculation over an idealized bed consisting of equally sized ripples with slightly uneven spacing (Figure 10c) suggests a mechanism for this amplification of sinuosity. In a flow corresponding to the equilibrium condition ($\lambda/d = 0.65$), the peaks in time-averaged bed shear stress are of similar magnitude for all crests under both flow directions (Figure 10d). Asymmetries in the gradient of shear stress across peaks indicate that the widely spaced pair of ripples will migrate toward one another and the closely spaced pair will migrate away from one another (ripples migrate in the direction of gentler shear stress gradient), evening out the ripple spacing. A flow with a larger orbital diameter ($\lambda/d = 0.36$), which will widen the average ripple spacing, has the opposite effect: the crest bed shear stress is asymmetric (Figure 10d), driving the widely spaced ripple pair farther apart and the closely spaced pair closer together. The asymmetric shear stress arises because the flow accelerates more in a wider trough, generating larger stress as it approaches the crest. When crests preferentially migrate toward the closest adjacent crest, any initial perturbations in the ripple wavelength along a ripple crest will be amplified. We propose that this process leads to the observed crest sinuosity, or bulging pattern, with shorter-wavelength bulges presumably being damped by diffusion-like crest-parallel sand transport [*Rubin*, 2012].

As crests grow more sinuous, they break up into fragments, and the average ripple wavelength lengthens because some of these fragments disappear. We analyzed the wave tank experiments to find out what causes crests to disappear (Figure 10a). The ripple that is eventually annihilated does not initially have the lowest peak, but it is adjacent to a tall ripple that produces long separation zones containing large separation vortices that erode neighboring crests. The calculated shear stress divergence over the bed (Figure 10b) shows that the deposition rate on the doomed crest diminishes rapidly once its height begins to shrink. This is consistent with earlier observations by *Marieu et al.* [2008], who noted that differences in ripple heights are amplified, causing slightly smaller ripples to disappear. As the ripple disappears, its two neighboring crests migrate toward one another through the mechanism described above, producing a final bed profile with nearly uniform ripple spacing.

Our explanation for the development of a bulging pattern through the amplification of irregularities in crest height and spacing differs from other proposed explanations. *Hansen et al.* [2001] remarked that separation zone vortices might be prone to Rayleigh-Plateau instabilities, in which the vortex

breaks up into along-crest segments with a characteristic wavelength, leading to bulging crests. However, this vortex roll instability does not necessarily explain why bulging crests would only appear when $\lambda/d < 0.65$. Our flow calculations show that irregularities in crest spacing are stable for equilibrium conditions and unstable for widening crests, which predicts that bulging and associated merging [*Doucette and O'Donoghue*, 2006] should only happen if $\lambda/d < 0.65$. Our two-dimensional flow models make no predictions about the characteristic along-crest length scale of the bulging instability, however.

3.4. Application to Bed Form Evolution Models

One of the main challenges in constructing bed form evolution models is the need to characterize complex interactions of a turbulent flow with evolving bed topography. The morphodynamic couplings explored here provide a physical basis for parameterizing the fluid flow in bed form evolution models. Both idealized [*Paarlberg et al*., 2009] and predictive [*Paarlberg et al*., 2010] models in current-dominated environments commonly employ parameterizations of the separation zone [*Engel*, 1981]. These dynamics become increasingly complicated in unsteady flows. Parameterizing the effect of the separation zone on wavelength selection of equilibrium and transient wave ripples could contribute to the development of improved models of bed form morphodynamics. For example, we envision a simple function relating orbital diameter, ripple height, and separation zone length that could be used to compute the location and growth rate of incipient crests and the migration or decay of existing crests. Applying such a parameterization to along-crest differences in ripple height and spacing would lead to a quasi two-dimensional (map view) model that could be compared with observed ripple defects and transient ripple patterns. Understanding the origins of ripple defects would make it possible to extract information about transient flow conditions from two-dimensional ripple patterns in modern sediment and ancient strata. A simple flow parameterization would also allow efficient modeling of bed form evolution over large spatial domains and long time intervals, which would enable, for example, bed roughness estimates relevant to coastal engineering.

4. Conclusions

We used wave tank experiments and a lattice Boltzmann numerical flow model to study two phenomena in orbital wave ripples: the mechanism that selects the equilibrium ripple wavelength and large-scale symmetry breaking during transient adjustment of ripple fields. We observe that the extensively documented ratio of 0.65 between the equilibrium ripple wavelength and the flow orbital diameter is set by the maximum length of the separation zone downstream of a ripple crest and that the equilibrium ratio maximizes the bed shear stress that transports sand from troughs to ripple crests. When the wave orbital diameter is shortened, two secondary crests appear in every trough, but only one grows to full size. We find that incipient secondary crests on the upstream sides of ripples act as "speed bumps" that shorten the separation zones on the downstream sides and that this causes secondary crests on the same side, either right or left, to prevail in every trough. When the wave orbital diameter is lengthened, ripples develop a bulging pattern in which some parts of adjacent crests move closer together and other parts move farther apart. We find that the effect of uneven ripple spacing on bed shear stress makes each section of a ripple crest migrate preferentially toward the nearest adjacent crest, which should amplify any initial crest sinuosity and may explain the observed bulging instability. Understanding the mechanisms that govern ripple equilibrium and adjustment provides insight into bed form dynamics and paleoenvironmental reconstructions and should aid in the development of morphodynamic models by providing a basis for parameterizing complicated flow effects.

Appendix A: Comparison of Lattice Boltzmann Model to Analytical Solutions, Laboratory Experiments, and Other Computational Methods

A1. Comparison to Analytical Solution for Plane Poiseuille Flow

We compared our lattice Boltzmann numerical flow model to the analytical solution for flow driven by a pressure gradient G (Pa m^{-1}) between two parallel, no-slip walls, also called plane Poiseuille flow.

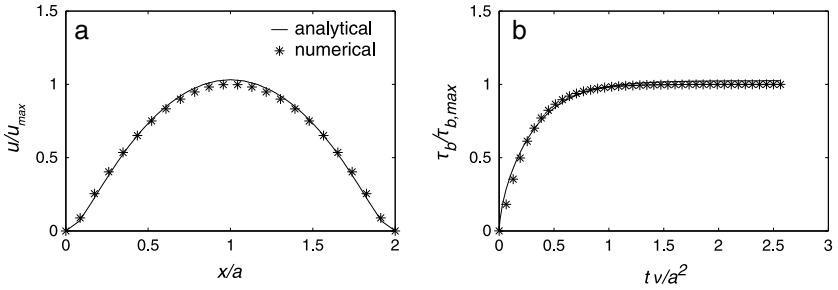

Figure A1. Comparison of lattice Boltzmann flow simulation with analytical solution for Poiseuille flow. (a) Steady state parabolic velocity profile (equation (A1)). (b) Time evolution of the boundary shear stress toward the equilibrium value (equation (A2)).

At equilibrium, the driving force equals the dissipation due to boundary shear stress, and the flow velocity u (m s^{-1}) maintains a parabolic shape (Figure A1a) given by

$$u(x) = -\frac{G}{2\mu}x(2a - x), \tag{A1}$$

where μ is the dynamic viscosity (10^{-3} Pa s for water at 20°C) and a (m) is half the distance between the walls [*Batchelor*, 2000]. Starting from rest, the wall shear stress as a function of time, $\tau_b(t)$ (N m^{-2}), is given by

$$\tau_b(t) = Ga\left[1 - 8\sum_{n=1}^{\infty}\frac{1}{\lambda_n^3 J_1(\lambda_n)}\exp\left(-\lambda_n^2\frac{\nu t}{\sqrt{2}a^2}\right)\right], \tag{A2}$$

where J_1 is the Bessel function of the first kind of order 1, λ_n is the nth positive root of $J_0(\lambda) = 0$, t is the time in seconds, and ν is the kinematic viscosity (m^2 s^{-1}). We derived this equation from the analytical solution of velocity in a pipe given by *Batchelor* [2000, equation (4.3.19)]. The factor $\sqrt{2}$ is used to convert from polar (pipe flow) to Cartesian (plane flow) coordinates. At $t = \infty$, the wall shear stress is $\tau_{b,\max} = Ga$.

We modeled flow for 10 s between two plates 2.5 mm apart using a pressure gradient of 0.01 Pa m^{-1}, $\overline{x} = 0.1$ mm, and $\overline{t} = 2 \cdot 10^{-6}$ s. Bottom and top boundary conditions were no-slip, and left and right boundaries were periodic. The final flow velocity (Figure A1a) and bed shear stress deviate less than 2% from the analytical predictions, and the time evolution of the bed shear stress (Figure A1b) follows the trend predicted by equation (A2).

A2. Comparison to Flume Measurements

To test the turbulent flow predictions of our lattice Boltzmann model, we compared the simulated velocity field directly to the detailed particle image velocimetry (PIV) flume measurements made by *Van der Werf et al.* [2007, Figure 2, experiment Mr5b50]. In their experiment, the ripples have an average wavelength of 0.46 m and an average height of 0.078 m, the free-stream flow velocity is 0.48 m s^{-1}, the wave period is 5 s, and the orbital diameter 0.76 m. The PIV measurements used suspended sand as the seeding agent [*van der Werf et al.*, 2007].

We modeled 10 flow oscillations with $\overline{x} = 2$ mm and $\overline{t} = 2 \cdot 10^{-5}$ s using the same bed profile as shown in their Figure 2 [*van der Werf et al.*, 2007], but linearly interpolated between the right and left sides of the ripple to allow for periodic boundary conditions. We compared 66 flow profiles from our lattice Boltzmann model phase averaged over 10 wave cycles with 66 flow profiles from the flume experiment phase averaged over 4 wave cycles.

A visual comparison of the numerical and experimental flow structures (Figure A2) reveals that the flume measurements (Figure A2, left) appear to have fewer turbulent velocity fluctuations far from the bed than our simulations (Figure A2, right). Flow structures close to the bed, especially those associated with the development of separation vortices (red ellipses in Figure A2) compare well. The velocity magnitudes and the horizontal length scales of the separation vortices are similar and the times at which they occur coincide.

The numerical flow velocities show good quantitative agreement with the experimental measurements and indicate no systematic underprediction or overprediction (Figure A3). The velocity maxima in the LBM simulations are slightly higher, which may be due partly to inertia of the suspended sediment in the laboratory experiments. Flow reversal velocities (circled areas in Figure A3) and free-stream velocities (inset in Figure A3) correspond well.

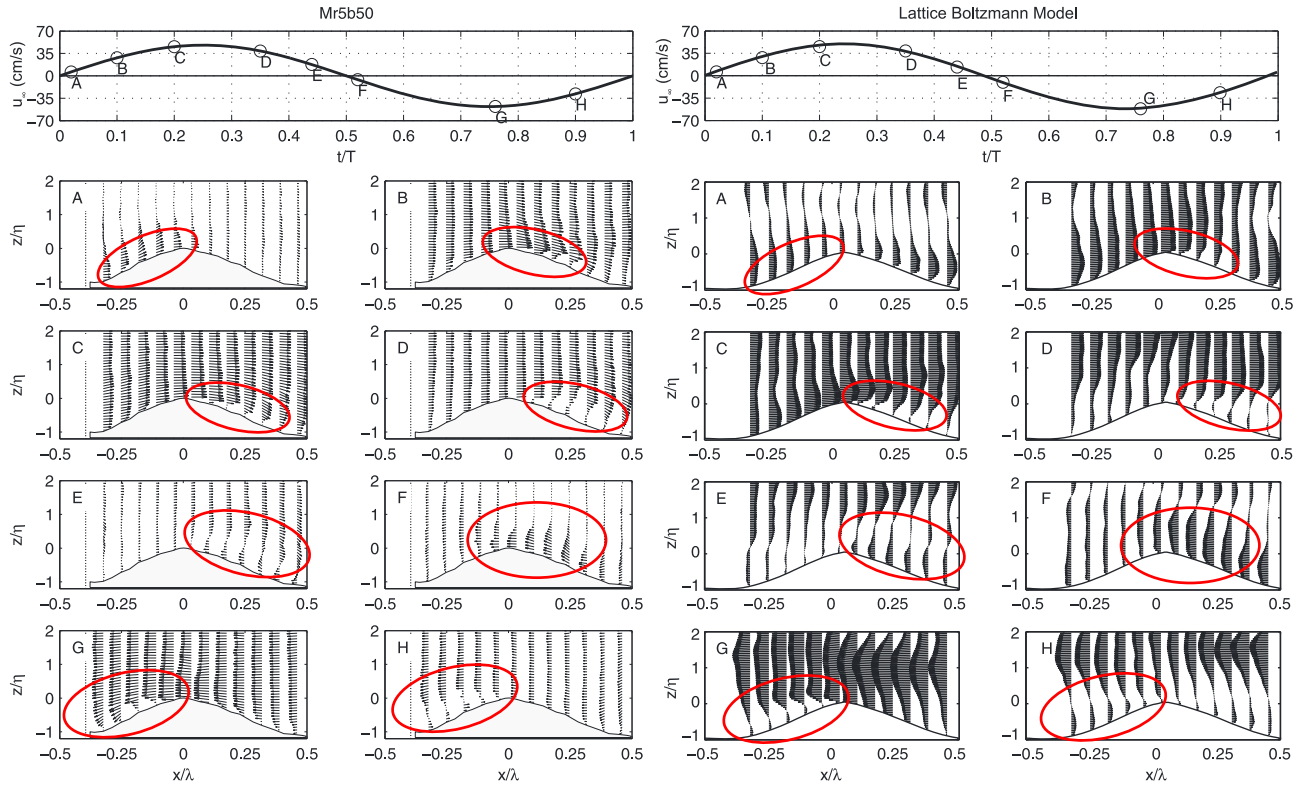

Figure A2. Velocity field for eight phases of a typical flow oscillation. (left) Experiment Mr5b50 of *van der Werf et al.* [2007]. (right) Numerical results obtained from the LBM simulation. Red ovals outline areas of interest close to the bed. The horizontal spacing of the vertical columns of velocity vectors corresponds to a velocity of 0.8 m s^{-1}.

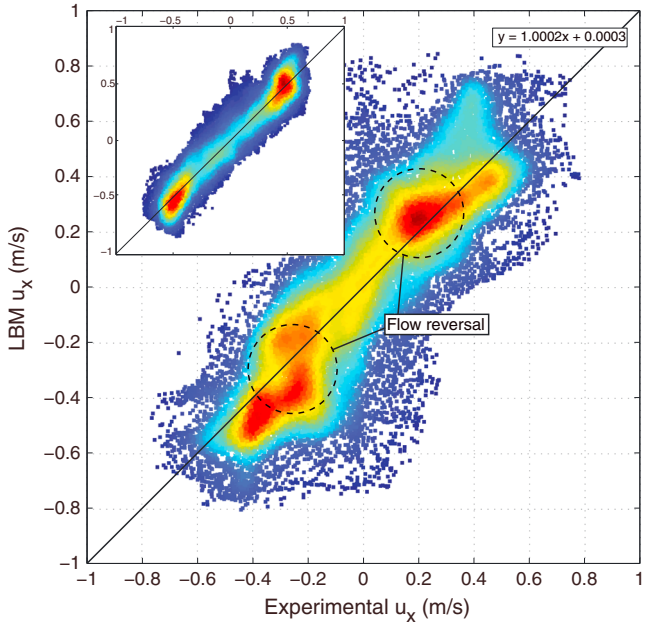

Figure A3. Direct comparison of near-bed ($z < \eta$) horizontal velocities from experiment Mr5b50 reported in *Van der Werf et al.* [2007] with those obtained from the LBM. Colors indicate data density. The black line is the least squares best fit, which is very close to a 1:1 line. Dashed circles are the velocities associated with flow reversal. Inset shows the horizontal velocities above the crest ($z > \eta$) and a least squares fit to those data.

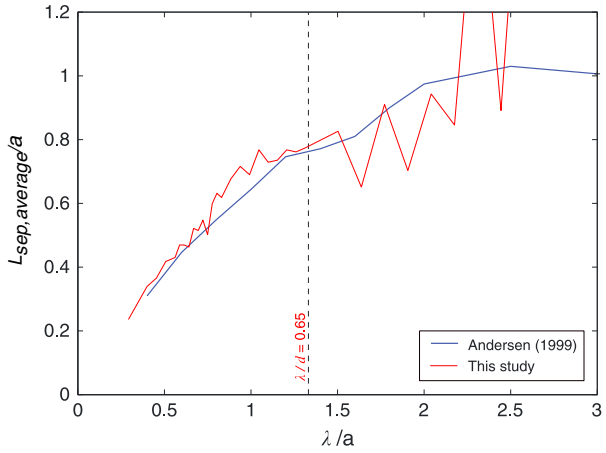

Figure A4. Comparison of separation zone lengths from RANS simulations of *Andersen* [1999, Figure 4.8] and our lattice Boltzmann simulations. Modified from *Andersen* [1999]. Dotted line shows $\lambda/d = 0.65$.

A3. Comparison of LBM to Results From a RANS Fluid Dynamical Model

We are not aware of any direct experimental or field measurements of the time evolution of bed shear stress on ripples under oscillatory flow that are sufficiently detailed to permit comparisons with our flow simulations. To evaluate the bed shear stress predictions from the LBM, we therefore compared our simulation results to a conventional flow model based on the Reynolds-averaged Navier-Stokes (RANS) equations [*Andersen*, 1999]. *Andersen* [1999] computed the average (not maximum) horizontal length of the separation zone ($L_{sep,average}$) while varying the ratio of the ripple wavelength to orbital amplitude ($a = ½\ d$). To calculate $L_{sep,average}$, we used the simulations described in section 3.1.1 (Figures 6b and 7d), in which the free-stream flow velocity is 0.1 m s^{-1}, the wave period is 2.5 s, and the orbital diameter is 0.077 m. We modeled flow oscillations with $\overline{x} = 1$ mm and $\overline{t} = 10^{-5}$ s and computed $L_{sep,average}$ by averaging the size of the separation zone through half a wave cycle.

Our results differ slightly from those of *Andersen* [1999], and generally show more variability, but the values and trend are very similar, especially for flows close to the equilibrium value of $\lambda/d \approx 0.65$ ($\lambda/a \approx 1.3$) (Figure A4). The differences may be partly explained by different methods for calculating the average length of the separation zone.

Appendix B: Sensitivity of Lattice Boltzmann Model to Grid Resolution

We performed grid resolution sensitivity tests for our lattice Boltzmann flow simulations by measuring the maximum separation zone length ($L_{sep,max}$) for the same set of flow parameters while varying the grid resolution. For every model run, the wave period was 2 s, the orbital diameter was 0.1 m, and the ripple wavelength was 0.075 m, with the ripple profile given by equation (13). We varied $\overline{x}$ between 1.5 mm (with $N_x = N_y = 50$) and 0.625 mm (with $N_x = N_y = 120$) while keeping $\overline{t} = 0.01\overline{x}$ to maintain a constant Mach number. Maximum separation zone length was measured over 30 half cycles using the procedure described in section 2.2.2. The resulting values of L_{sep} show no systematic trend with grid resolution and are within uncertainty of one another, indicating that the separation zone length is insensitive to grid resolution (Figure B1).

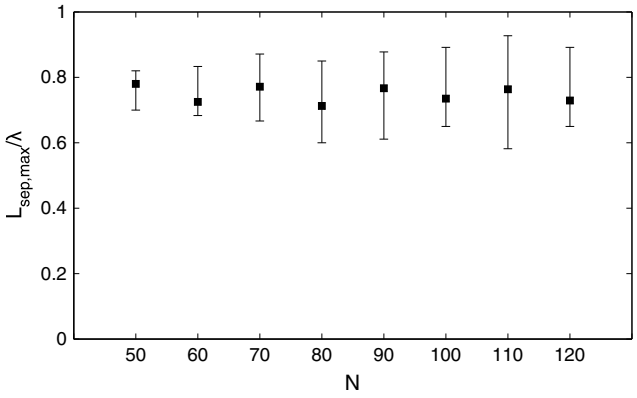

Figure B1. Plot of median separation zone length over 30 half cycles for different grid resolutions, with *N* indicating the number of points along the horizontal and vertical dimension of the grid. The error bars indicate the 95% confidence interval of the median.

Acknowledgments
The data for this paper are available upon request from the authors. This study was supported by the U.S. National Science Foundation through awards EAR-1225865 to J.T.P. and EAR-1225879 to P.M.M. We thank Kim Huppert, Abby Koss, John Southard, Mike Szulczewski, Jocelyn Fuentes, Mathieu Lapôtre, and Tom Ashley for assistance with wave tank construction and experiments. Andy Wickert designed and built the magnetic trigger used to perform time-lapse photography. We thank Jebbe van der Werf for sharing his PIV data. We are grateful to Peter Traykovski, John Southard, Ryan Ewing, and Mauricio Perillo for discussions of wave ripples. The Editor, Associate Editor, and three anonymous reviewers made suggestions that helped us improve the paper.

References

Aidun, C. K., and J. R. Clausen (2010), Lattice-Boltzmann method for complex flows, *Annu. Rev. Fluid Mech.*, *42*, 439–472, doi:10.1146/annurev-fluid-121108-145519.

Allen, P. A., and P. F. Hoffman (2005), Extreme winds and waves in the aftermath of a Neoproterozoic glaciation, *Nature*, *433*(7022), 123–127, doi:10.1038/nature03176.

Andersen, K. H. (1999), The dynamics of ripples beneath surface waves, PhD thesis, Niels Bohr Institute, Univ. of Copenhagen, Copenhagen.

Bagnold, R. A., and G. Taylor (1946), Motion of waves in shallow water. Interaction between waves and sand bottoms, *Proc. R. Soc. London. Ser. A. Math. Phys. Sci.*, *187*(1008), 1–18, doi:10.1098/rspa.1946.0062.

Batchelor, G. K. (2000), *An Introduction to Fluid Dynamics*, Cambridge Univ. Press, Cambridge, U. K.

Bouzidi, M., M. Firdaouss, and P. Lallemand (2001), Momentum transfer of a Boltzmann-lattice fluid with boundaries, *Phys. Fluids*, *13*(11), 3452, doi:10.1063/1.1399290.

Cabot, W., and P. Moin (2000), Approximate wall boundary conditions in the large-eddy simulation of high Reynolds number flow, *Flow, Turbul. Combust.*, *63*(1–4), 269–291, doi:10.1023/A:1009958917113.

Cappietti, L. (2006), Lattice Boltzmann numerical simulations of wave-current interaction within the boundary layer, in *Coastal Dynamics 2005*, pp. 1–13, American Society of Civil Engineers, Reston, Va.

Cappietti, L., and B. Chopard (2006), A Lattice Boltzmann study of the 2D boundary layer created by an oscillating plate, *Int. J. Mod. Phys. C*, *17*, 39–52, doi:10.1142/S0129183106008820.

Chen, S., and G. D. Doolen (1998), Lattice Boltzmann method for fluid flows, *Annu. Rev. Fluid Mech.*, *30*(1), 329–364, doi:10.1146/annurev.fluid.30.1.329.

Chou, Y.-J., and O. B. Fringer (2010), A model for the simulation of coupled flow-bed form evolution in turbulent flows, *J. Geophys. Res.*, *115*(C10), C10041, doi:10.1029/2010JC006103.

Clifton, H. E., and J. R. Dingler (1984), Wave-formed structures and paleoenvironmental reconstruction, *Mar. Geol.*, *60*, 165–198, doi:10.1016/0025-3227(84)90149-X.

Dong, Y., P. Sagaut, and S. Marie (2008), Inertial consistent subgrid model for large-eddy simulation based on the lattice Boltzmann method, *Phys. Fluids*, *20*(3), 035104, doi:10.1063/1.2842379.

Doucette, J. S., and T. O'Donoghue (2006), Response of sand ripples to change in oscillatory flow, *Sedimentology*, *53*(3), 581–596, doi:10.1111/J.1365-3091.2006.00774.X.

Engel, P. (1981), Length of flow separation over dunes, *J. Hydraul. Div.*, *107*(10), 1133–1143.

Evans, O. F. (1943), Effect of change of wave size on the size and shape of ripple marks, *J. Sediment. Res.*, *13*(1), 35–39, doi:10.1306/D4269189-2B26-11D7-8648000102C1865D.

Evans, O. F. (1949), Ripple marks as an aid in determining depositional environment and rock sequence, *J. Sediment. Res.*, *19*(2), 82–86, doi:10.1306/D426935A-2B26-11D7-8648000102C1865D.

Grant, W. D., and O. S. Madsen (1982), Movable bed roughness in unsteady oscillatory flow, *J. Geophys. Res.*, *87*(C1), 469–481, doi:10.1029/JC087iC01p00469.

Hansen, J. L., M. van Hecke, A. Haaning, C. Ellegaard, K. H. Andersen, T. Bohr, and T. Sams (2001), Pattern formation: Instabilities in sand ripples, *Nature*, *410*(6826), 324, doi:10.1038/35066631.

Jerolmack, D. J., and D. Mohrig (2005), A unified model for subaqueous bed form dynamics, *Water Resour. Res.*, *41*(12), w12421, doi:10.1029/2005WR004329.

Lallemand, P., and L. S. Luo (2000), Theory of the lattice Boltzmann method: Dispersion, dissipation, isotropy, Galilean invariance, and stability, *Phys. Rev. E*, *61*(6), 6546–6562, doi:10.1103/PhysRevE.61.6546.

Lallemand, P., and L. S. Luo (2003), Lattice Boltzmann method for moving boundaries, *J. Comput. Phys.*, *184*(2), 406–421, doi:10.1016/s0021-9991(02)00022-0.

Lamb, M. P., W. W. Fischer, T. D. Raub, J. T. Perron, and P. M. Myrow (2012), Origin of giant wave ripples in snowball Earth cap carbonate, *Geology*, *40*(9), 827–830, doi:10.1130/G33093.1.

Lofquist, K. E. B. (1978), *Sand Ripple Growth in an Oscillatory-Flow Water Tunnel*, U.S. Army, Corps of Engineers, Fort Belvoir, Va.

Longuet-Higgins, M. S. (1981), Oscillating flow over steep sand ripples, *J. Fluid Mech.*, *107*, 1–35, doi:10.1017/S0022112081001651.

Marieu, V., P. Bonneton, D. L. Foster, and F. Ardhuin (2008), Modeling of vortex ripple morphodynamics, *J. Geophys. Res.*, *113*, C09007, doi:10.1029/2007JC004659.

Miller, M., and P. D. Komar (1980), Oscillation sand ripples generated by laboratory apparatus, *J. Sediment. Res.*, *50*(1), 173–182.

Nielsen, P. (1981), Dynamics and geometry of wave-generated ripples, *J. Geophys. Res.*, *86*(C7), 6467–6472, doi:10.1029/JC086iC07p06467.

Paarlberg, A. J., C. M. Dohmen-Janssen, S. Hulscher, and P. Termes (2009), Modeling river dune evolution using a parameterization of flow separation, *J. Geophys. Res.*, *114*, F01014, doi:10.1029/2007JF000910.

Paarlberg, A. J., C. M. Dohmen-Janssen, S. Hulscher, P. Termes, and R. Schielen (2010), Modelling the effect of time-dependent river dune evolution on bed roughness and stage, *Earth Surf. Processes Landforms*, *35*(15), 1854–1866, doi:10.1002/esp.2074.

Pedocchi, F., and M. H. García (2009a), Ripple morphology under oscillatory flow: 1. Prediction, *J. Geophys. Res.*, *114*, C12014, doi:10.1029/2009JC005354.

Pedocchi, F., and M. H. García (2009b), Ripple morphology under oscillatory flow: 2. Experiments, *J. Geophys. Res.*, *114*, C12015, doi:10.1029/2009JC005356.

Piomelli, U. (2008), Wall-layer models for large-eddy simulations, *Prog. Aerosp. Sci.*, *44*(6), 437–446, doi:10.1016/j.paerosci.2008.06.001.

Piomelli, U., and E. Balaras (2002), Wall-layer models for large-eddy simulations, *Annu. Rev. Fluid Mech.*, *34*(1), 349–374, doi:10.1146/annurev.fluid.34.082901.144919.

Rubin, D. M. (2012), A unifying model for planform straightness of ripples and dunes in air and water, *Earth Sci. Rev.*, *113*(3–4), 176–185, doi:10.1016/j.earscirev.2012.03.010.

Scherer, M. A., F. Melo, and M. Marder (1999), Sand ripples in an oscillating annular sand-water cell, *Phys. Fluids*, *11*, 58, doi:10.1063/1.869902.

Schnipper, T., K. Mertens, C. Ellegaard, and T. Bohr (2008), Amplitude equation and long-range interactions in underwater sand ripples in one dimension, *Phys. Rev. E*, *78*(4), 47301, doi:10.1103/PhysRevE.78.047301.

Sekiguchi, T. (2005), Ripples with secondary crests as a possible indicator of palaeo-wave direction: A laboratory experiment, *J. Geol. Soc. Japan*, *111*(3), 182–186.

Sekiguchi, T., and T. Sunamura (2004), A laboratory study of formative conditions for characteristic ripple patterns associated with a change in wave conditions, *Earth Surf. Processes Landforms*, *29*(11), 1431–1435, doi:10.1002/esp.1139.

Shulyak, B. A. (1963), Periodic bottom structures of wave flow, *Deep Sea Res. Oceanogr. Abstr.*, *10*(4), 488–497, doi:10.1016/0011-7471(63)90512-6.

Smith, D., and J. F. A. Sleath (2005), Transient ripples in oscillatory flows, *Cont. Shelf Res.*, *25*(4), 485–501, doi:10.1016/j.csr.2004.10.012.

Squyres, S. W., et al. (2004), In situ evidence for an ancient aqueous environment at Meridiani Planum, Mars, *Science*, *306*(5702), 1709–1714, doi:10.1126/science.1104559.

Stokes, G. G. (1851), On the effect of the internal friction of fluids on the motion of pendulums, *Camb. Philos. Soc. Trans.*, *9*, 8–106.

Traykovski, P., A. E. Hay, J. D. Irish, and J. F. Lynch (1999), Geometry, migration, and evolution of wave orbital ripples at LEO-15, *J. Geophys. Res.*, *104*(C1), 1505–1524, doi:10.1029/1998JC900026.

Van der Werf, J. J., J. S. Doucette, T. O'Donoghue, and J. S. Ribberink (2007), Detailed measurements of velocities and suspended sand concentrations over full-scale ripples in regular oscillatory flow, *J. Geophys. Res.*, *112*, F02012, doi:10.1029/2006JF000614.

Wiberg, P. L., and C. K. Harris (1994), Ripple geometry in wave-dominated environments, *J. Geophys. Res.*, *99*, 775–790, doi:10.1029/93JC02726.